

CONDENSED MATTER PHYSICS

Signatures of a spin-active interface and a locally enhanced Zeeman field in a superconductor-chiral material heterostructure

Cliff Chen¹†, Jason Tran¹†, Anthony McFadden², Raymond Simmonds², Keisuke Saito³, En-De Chu¹, Daniel Morales¹, Varrick Suezaki¹, Yasen Hou^{4,5}, Joe Aumentado², Patrick A. Lee⁴, Jagadeesh S. Moodera^{4,5}, Peng Wei¹*

A localized Zeeman field, intensified at heterostructure interfaces, could play a crucial role in a broad area including spintronics and unconventional superconductors. Conventionally, the generation of a local Zeeman field is achieved through magnetic exchange coupling with a magnetic material. However, magnetic elements often introduce defects, which could weaken or destroy superconductivity. Alternatively, the coupling between a superconductor with strong spin-orbit coupling and a nonmagnetic chiral material could serve as a promising approach to generate a spin-active interface. Here, we leverage an interface superconductor, namely, induced superconductivity in noble metal surface states, to probe the spin-active interface. Our results unveil an enhanced interface Zeeman field, which selectively closes the surface superconducting gap while preserving the bulk superconducting pairing. The chiral material, i.e., trigonal tellurium, also induces Andreev bound states (ABS) exhibiting spin polarization. The field dependence of ABS manifests a substantially enhanced interface Landé *g*-factor ($g_{eff} \sim 12$), thereby corroborating the enhanced interface Zeeman energy.

Copyright © 2024 The Authors, some rights reserved; exclusive licensee American Association for the Advancement of Science. No claim to original U.S.
Government Works.
Distributed under a Creative Commons Attribution
NonCommercial
License 4.0 (CC BY-NC).

INTRODUCTION

Heterostructures combining a structurally chiral material with a superconductor have recently unveiled unique features of induced spin polarization at the superconductor interface (1) and quasiparticle states of magnetic origin (2-5). The underlying mechanism is intricately associated with chirality-induced spin selectivity (CISS), a phenomenon that connects the structural chirality to the orbital angular momentum and spin of electrons. Although the theoretical framework of CISS is evolving, recent models and experimental investigations have underscored the imperative role of spin-orbit coupling (SOC) in facilitating the conversion of chirality-induced orbital polarization of an electron into spin polarization (6-8). In the context of superconductivity, therefore, obtaining an interface superconductor with strong SOC is highly desirable to elucidate the manifestation of CISS and would be crucial for superconducting spintronics and topological superconductivity (9). Furthermore, because CISS is an interface phenomenon, the quality of the interface is critical. In contrast to previous reports, where the interface is constructed ex situ by integrating a superconductor with organic chiral molecules (1-5), an interface constructed under ultrahigh vacuum (UHV) is desired. Such an interface may substantially enhance the Zeeman energy at the surface of a superconductor, which could serve as a candidate for creating unconventional quasiparticles such as Majorana bound states (10, 11). The spin-active interface may also lead to well-defined spin-polarized quasiparticle bound states, i.e., Andreev bound states (ABS), suitable for constructing an Andreev spin qubit.

RESULTS

By leveraging proximity effect, we induce superconductivity into a (111)-oriented Au layer, i.e., Au(111), to obtain a surface superconductor with strong SOC. We make Au(111) thin with the aim to acquire a full superconducting gap from an epitaxially grown superconductor layer underneath (Fig. 1A). The Au(111) layer is expected to host Shockley surface states, which become superconducting due to the proximity effect and may be used to sense any local Zeeman field once an interface is formed on top (12, 13). We synthesize high-quality Au(111)/Nb bilayers (Materials and Methods and section S1). The crystallinity, sharp interface, and ultrathin layers are confirmed by grazing incidence x-ray diffraction (GIXRD) and in situ electron diffraction characterizations (Fig. 1A and section S1). The results demonstrate a substantially improved layer quality compared to the previously reported Au(111)/V materials (12–14). Because of strong SOC, the layers break the Pauli paramagnetic limit. Figure 1B shows the in-plane upper critical field $(H_{C,\parallel})$ of Au(111)/Nb samples with varying Nb and Au thicknesses. When both Nb and Au(111) are thin, we obtain $H_{C,\parallel} > H_P$. Here, H_P is the

Pauli paramagnetic limit defined as $H_P = \frac{\Delta}{\sqrt{2}\mu_B}$ (Δ is the supercon-

ducting gap and μ_B is the Bohr magneton) to account for the pair breaking energy when the magnetic field acts on the spin of the quasiparticles and when SOC is negligible (15). When SOC is considered, we adopt the implicit relation describing the pair breaking mechanism (15, 16)

$$\ln \frac{T_C}{T_{C0}} = \psi\left(\frac{1}{2}\right) - \psi\left(\frac{1}{2} + \frac{\alpha}{2\pi k_B T_C}\right) \tag{1}$$

Here, α is the pair-breaker strength (or pair breaking energy) defined as $2\alpha = \frac{\hbar}{\tau_k}$, with τ_k being the lifetime of the Cooper pairs. T_{C0} is T_C under zero applied field and ψ is the digamma function. In the presence of a planar field H and spin-orbit scattering, $2\alpha = \hbar \tau_{SO} \left(\frac{2\mu_B H}{\hbar} \right)^2$

¹Department of Physics and Astronomy, University of California, Riverside, CA 92521, USA. ²National Institute of Standards and Technology, Boulder, CO 80305, USA. ³Rigaku Americas, a Division of Rigaku Americas Holding, The Woodlands, TX 77381, USA. ⁴Department of Physics, Massachusetts Institute of Technology, Cambridge, MA 02139, USA. ⁵Francis Bitter Magnet Laboratory, and Plasma Science and Fusion Center, Massachusetts Institute of Technology, Cambridge, MA 02139, USA.

^{*}Corresponding author. Email: peng.wei@ucr.edu

[†]These authors contributed equally to this work.

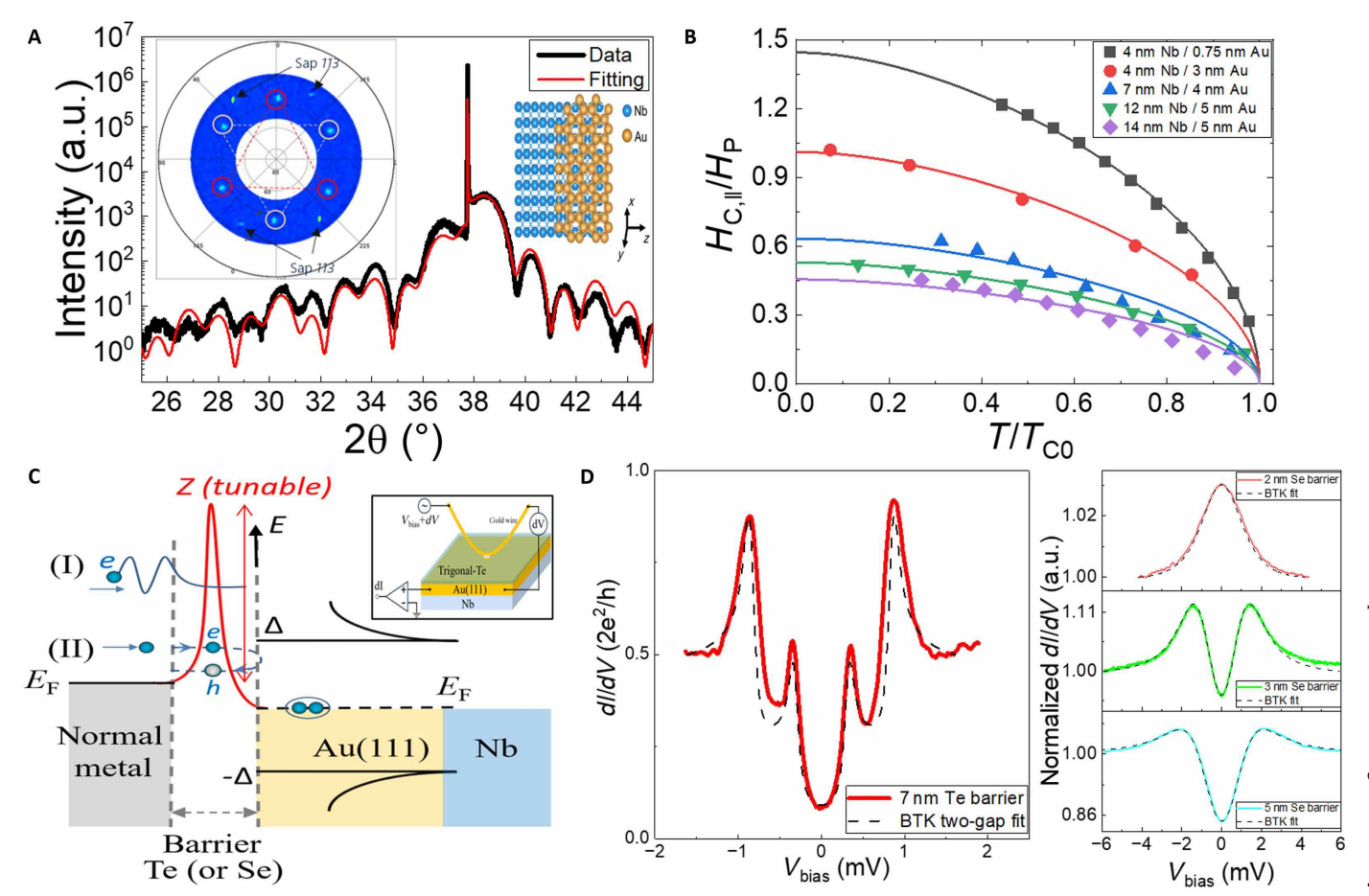


Fig. 1. Superconductor with strong spin-orbit coupling (SOC), signatures of the induced surface superconducting gap, and tunneling to Au(111) surface using tunnel barriers with adjustable properties. (A) GIXRD $2\theta - \omega$ scan. The main diffraction peak is at around $2\theta \sim 38.5^{\circ}$, which manifests itself as overlapped Nb(110) and Au(111) peaks. The fringes/beatings reflect the thicknesses of the layers and are fitted using dynamical simulation fittings (red curve). Inset (left) shows the x-ray pole figure scan confirming the (111)-oriented gold surface. The schematic layout of the Au(111) and Nb(110) is shown in the inset (right). (B) The in-plane upper critical field $H_{C,\parallel}$ is plotted against temperature in samples with a variety of Au and Nb thicknesses. $H_{C,\parallel}$ is normalized to H_P and T is normalized to the critical temperature at zero field T_{CO} . Reducing the thicknesses of both Au and Nb increases $H_{C,\parallel}/H_P$. (C) A schematic of the quasiparticle reflection processes across the interface including ordinary reflection (tunneling) and Andreev reflection (section S2). A structure layout of the four-terminal point contact device is shown in the inset (Materials and Methods). (D) Left: The dl/dV spectrum measured using tellurium (Te) (7 nm) as a barrier on a Au(111) (15 nm)/Nb sample. The data are fitted (dotted line) using a two-gap BTK approach (sections S2 and S3). Right: Adjusting the barrier height on Au(111)/Nb using a similar low-gap semiconductor, i.e., selenium (Se), with varying Se thicknesses: 2 nm (top), 3 nm (middle), and 5 nm (bottom). The dotted line is the fit to the BTK theory with fitting results given in table S1.

holds with τ_{SO} denoting the spin-orbit scattering time. Thus, $\alpha = \frac{2\mu_B^2 H^2}{\Delta_{SO}}$, with $\Delta_{SO} = \frac{\hbar}{\tau_{SO}}$ defining the SOC splitting energy. Using Eq. 1, we fit the data in Fig. 1B and obtain $H_{C,\parallel}/H_P \sim 1.4$ for Au(111) (7.5 Å)/Nb (4 nm) with $\Delta_{SO} \sim 1.4$ meV. Because the heterostructure consists of both Au(111) and Nb and the SOC of Nb is small, the fitted value of Δ_{SO} may depend on Nb thickness. We expect larger Δ_{SO} when Nb is thinner. We would also like to note that breaking the Pauli paramagnetic limit would otherwise not be possible if the thin (4 nm) Nb layer was not protected by the air inert Au(111) layer from oxidization.

To create an interface between a chiral material and Au(111), we explore low gap semiconductors, such as selenium (Se) or tellurium (Te), as a tunnel barrier. These materials, i.e., Se and Te, are known to have a trigonal phase, which is structurally chiral (17). We carry out modified point contact measurements using normal metal leads and barriers with a variable thickness to probe the induced superconductivity in

Au(111) (Materials and Methods and Fig. 1C). The dI/dV spectra are described by the Blonder-Tinkham-Klapwijk (BTK) formalism (section S2) (15, 16). We show that the spectra are modifiable upon changing the thickness of the tunnel barrier—evolving toward the tunneling-dominated regime when the thickness increases, for example, in the Se barrier in Fig. 1D (right). The BTK fitting results are given in table S1 and discussed in section S2. However, because of the amorphous growth of the Se barrier, the quasiparticle lifetime broadening (Γ) is large (section S2), which obscures any subtle tunneling features that are narrow in energy.

Using an epitaxially grown Te barrier (Fig. 1D, left), we obtain tunneling spectra with a markedly reduced Γ , which is limited by temperature k_BT (section S2). Because Γ is reduced, sharp tunneling features reminiscent of two superconducting gaps are observed in a thick Au(111) layer (15 nm) (Fig. 1D, left). The energy of the larger gap agrees with the bulk superconducting gap estimated

from $\Delta \sim 1.76k_BT_C$ according to BCS model (15) and the measured $T_C = 6.3$ K. We fit Fig. 1D (left) using a sum of two BTK dI/dV conductance, namely, a two-gap approach (section S3), to include both the bulk (Δ_B) and surface (Δ_S) gaps. The fit reproduces the data over a wide range of $V_{\rm bias}$, yielding $\Delta_B \sim 0.85$ meV and $\Delta_S \sim 0.33$ meV, which exactly match the locations of the dI/dV peaks in Fig. 1D (left). Although signatures of Δ_S have been observed in Au(111) before (13), here Δ_S stands out much more pronounced. Figure 1D (left) precisely reproduces Potter and Lee's theory of induced surface superconductivity in Au(111) (18). Compared to the previous work where $\Delta_S \sim 0.38$ meV (13), here $\Delta_S \sim 0.33$ meV is comparable.

When a planar field μ_0H is applied, i.e., a magnetic field applied parallel to the thin film surface, Δ_B and Δ_S evolve with $\mu_0 H$ (Fig. 2A). The gaps get reduced and are accompanied by a weakening of the coherence peaks. Using the two-gap BTK model fitting, we reproduce the experimental data under all μ_0H (Fig. 2A). The fitting in Fig. 2A further confirms the two-gap picture, i.e., the coexistence of Δ_B and Δ_S . To better demonstrate how Δ_B and Δ_S evolve with $\mu_0 H$, we plot the dI/dV spectra as a function of V_{bias} and $\mu_0 H$ in a density plot (Fig. 2B). The closing of Δ_S is directly tied to the fill-up of the superconducting gap in the low V_{bias} regime (Fig. 2B). The coherence peaks corresponding to Δ_B also move in toward lower energies as $\mu_0 H$ increases. To quantify such a field dependence, we plot Δ_S and Δ_B against $\mu_0 H$ in Fig. 2C. Here, the values of Δ_S and Δ_B are deduced from the two-gap BTK fitting according to the data in Fig. 2A. There is a sharp contrast on their field dependence. Δ_S versus $\mu_0 H$ follows a square root dependence and is well fitted according to $\Delta_S \sim \sqrt{1 - \left(\frac{H}{H_C}\right)^2}$ (Fig. 2C), which describes the gap closing of a superconductor in the thin film limit, i.e., thickness

« penetration depth (15). This agrees with the two-dimensional nature of Δ_S . The square root fitting also outlines the gap in the low V_{bias} regime in Fig. 2B, which confirms that the fill-up of the gap corresponds to the closing of Δ_S . On the other hand, Δ_B versus $\mu_0 H$ does not follow the square root dependence (Fig. 2C), consistent with the bulk nature of Δ_B . From the fitting, we extract the surface gap (Δ_S) critical field ~2.1 T, whereas the critical field for Δ_B is larger (Fig. 2C). Although $\Delta_S < \Delta_B$ and one may expect smaller critical field for Δ_S , the critical field (~2.1 T) is too small compared to the Pauli paramagnetic limit using $H_P = \frac{\Delta_S}{\sqrt{2}\mu_B}$ and $\Delta_S \sim 0.33$ meV

(Figs. 1D, left, and 2A). This may suggest that Δ_S is experiencing a stronger depairing mechanism. However, to confirm it, one needs to make Δ_S and Δ_B comparable. Signatures of Δ_S are also observed in another sample with a 10-nm Au(111) (section S5).

To confirm that Δ_S and Δ_B are subject to different depairing mechanisms, we obtain $\Delta_S \approx \Delta_B$ in a thinner (5 nm) Au(111) sample. $\Delta_S \approx \Delta_B$ allows us to compare their field dependence (or depairing mechanism) side by side. Similarly, we carry out dI/dV measurements across an epitaxially grown Te barrier and control the Te thickness so that tunneling is dominated. At $\mu_0 H = 0$ T (Fig. 3A), dI/dV shows one pair of coherence peaks. However, the evolution of the dI/dV spectra under $\mu_0 H$ cannot be explained by a single superconducting gap. At low fields, the gap is very sensitive to $\mu_0 H$. The gap gets quickly filled up accompanied by a transition of the dI/dV spectra from a U-shape gap (Fig. 3, A and B) to a V-shape gap ($\mu_0 H \sim 3$ T, Fig. 3C). At higher fields (after the transition, or $\mu_0 H > 3$ T), the gap widens up again (Fig. 3D) and evolves back toward a U-shape gap compared to Fig. 3C. At high fields, the gap becomes robust and is nearly unresponsive to $\mu_0 H$, which is

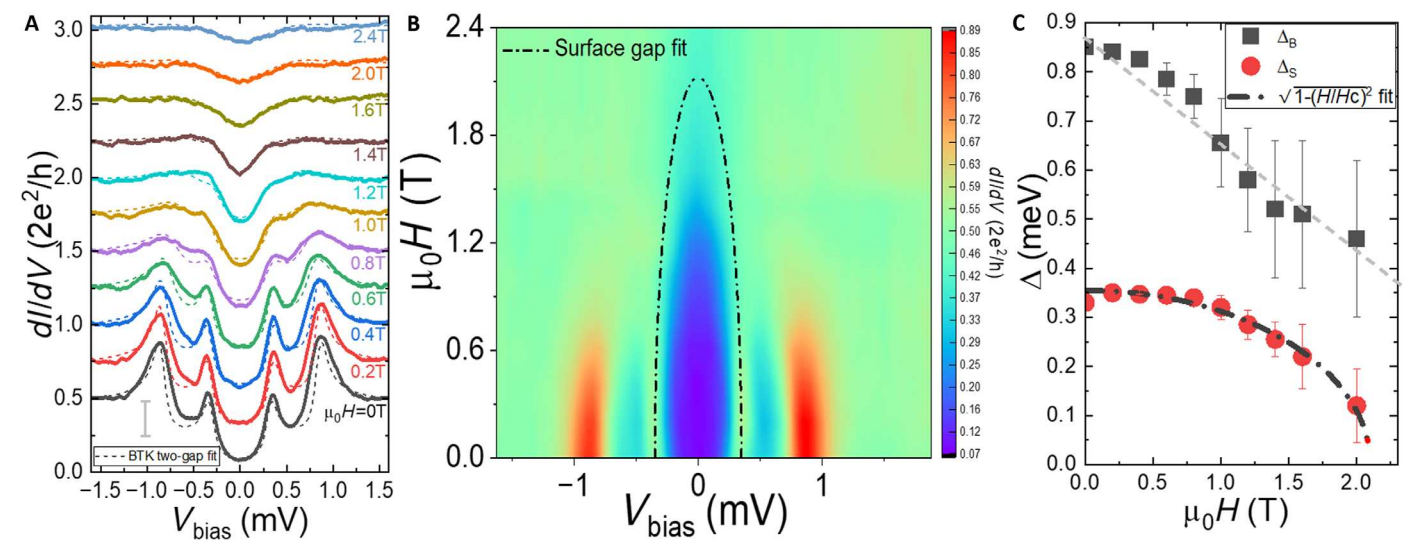


Fig. 2. Evolution of the bulk Δ_B and surface Δ_S superconducting gap under a planar magnetic field. (A) The fit to the dl/dV spectra using the two-gap BTK approach for various magnetic fields applied parallel to the Au(111)/Nb thin film sample. The sample (also shown in Fig. 1D, left) has a 15-nm-thick Au(111) layer and a 7-nm Te barrier. The gaps Δ_S and Δ_B are deduced from the fitting. The spectra are vertically shifted for clarity with a scale bar indicating $0.5 \, \mathrm{e}^2$ /h. (B) The density plot of the dl/dV data as a function of V_{bias} and $\mu_0 H$. The surface gap closes soon after a substantial fill-up of the superconducting gap (region in blue color). The dash-dot line shows the dependence of Δ_S versus $\mu_0 H$ following the fitting results in (C). (C) The evolution of Δ_S and Δ_B as a function of $\mu_0 H$. Here, Δ_S and Δ_B are deduced from the fitting in (A). The in-

creased error bar is due to the increased broadening under large fields. The dash-dot line (black) is the fitting results according to $\Delta_S \sim \sqrt{1-\left(\frac{H}{H_C}\right)^2}$ with the consideration

of the error bars. The fitting is consistent with the picture that Δ_S is the surface gap, which is two-dimensional in nature. The bulk gap Δ_B does not follow such a field dependence, and the dashed line (gray) is used to guide the eye. The critical field of Δ_S is smaller than that of Δ_B .

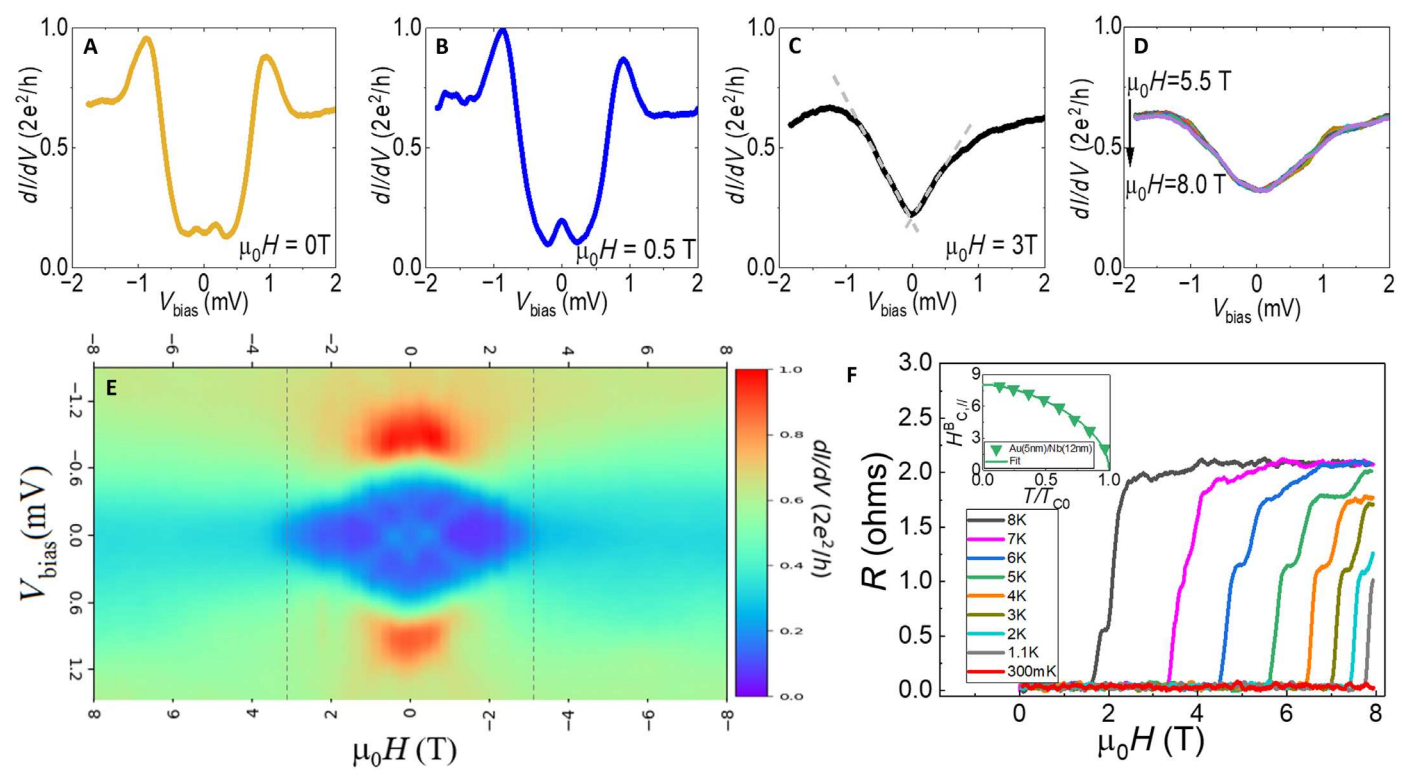
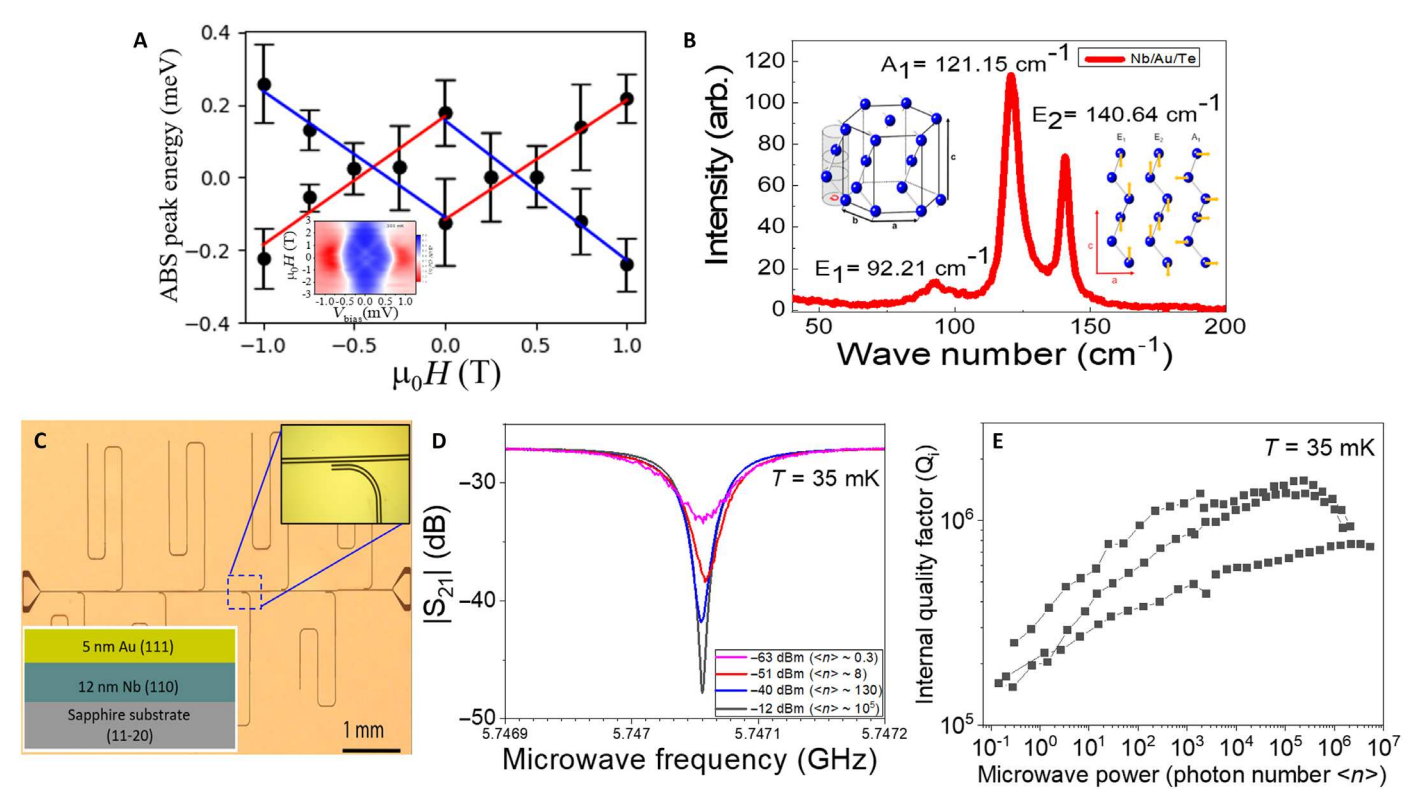


Fig. 3. Fast closing of Δ_S and signatures of an enhanced interface Zeeman field. (A to C) Characteristic dl/dV spectra under the planar μ_0H : 0 T, 0.5 T, and 3.0 T in a Au(111) (5 nm)/Nb with an epitaxial Te barrier. At 0 T (A), despite the two subtle tunneling peaks near $V_{bias} \sim 0$ mV (ABS in Fig. 4A), a single superconducting gap is observed. As μ_0H increases, the gap gets narrowed and filled up accompanied by an evolution from "U shape" in (A) and (B) to "V shape" in (C). The dotted line in (C) is used to guide the eye. (D) At high fields, the gap becomes nearly unresponsive to μ_0H , and the dl/dV spectra overlap in a wide range of fields (5.5 to 8.0 T). Compared to (C), the gap in (D) is widened and evolving back toward the "U shape." (E) dl/dV versus V_{bias} and μ_0H . Two gapped regimes are visible: one (dark blue regime) closes approximately at $\mu_0H \sim 3$ T, and the other one (light blue regime) survives up to $\mu_0H \sim 8$ T and beyond (also see D). The transition, i.e., the closing of the dark blue regime, is accompanied by the fill-up of the low field gap (also see A to C). At $\mu_0H \sim 0$ T, the two gaps overlap. (F) The simultaneous measurements of R versus μ_0H on the sample in (E). The sample is superconducting (red curve) throughout the whole magnetic field range. Inset: bulk critical field $H_{C,\parallel}^B$ versus T/T_{C0} . The fitting is based on Eq. 1.

demonstrated by an overlapped dI/dV spectra in a wide range of fields from $\mu_0 H \sim 5.5$ to 8.0 T (Fig. 3D). This implies that the low field gap and the high field gap have different origins. Furthermore, the transition between U- and V-shape dI/dV spectra signifies a nonconcurrent closing of multiple superconducting gaps, which has also been reported elsewhere, for example, in Au(111) with EuS islands (12). Therefore, Fig. 3 (A to D) agrees with the coexistence of two superconducting gaps in Au(111). Here, we note that the U- to V-shape transition is not due to other sub-gap states, which are resolvable in our high-resolution dI/dV measurements, for example, the ABS resolved in Figs. 3E and 4A. To better demonstrate the nonconcurrent gap closing, we carry out detailed dI/dV measurements as a function of μ_0H with a fine step field increment (Fig. 3E). The density plot in Fig. 3E clearly outlines the fill-up and closing of the low field gap, which resembles that in Fig. 2B. However, because $\Delta_S \approx \Delta_B$ at $\mu_0 H = 0$ T, the fast closing of Δ_S suggests that Δ_S is subject to a stronger depairing mechanism. To further prove that the high field gap (Fig. 3D) corresponds to the bulk gap (or Δ_B), we carry out simultaneous transport measurements (Fig. 3F). The fact that the sample resistance stays precisely at zero throughout the full scan of $\mu_0 H$ (Fig. 3F) confirms that the bulk sample is superconducting.

two-dimensional superconductor under a planar $\mu_0 H$. To describe the pair breaking, we recall Eq. 1. Because the pair breaking energy $2\alpha = \frac{\hbar}{\tau_k} = \frac{(2\mu_B H)^2}{\Delta_{SO}}$, we rewrite $\alpha = \frac{E_Z^2}{\mu_B H_{SO}}$ with $\Delta_{SO} = 2\mu_B H_{SO}$ and $E_Z = \mu_B H$. Here, E_Z is the corresponding Zeeman energy due to the applied field $\mu_0 H$, whereas H_{SO} is introduced as an effective field to account for SOC. Considering that superconductivity is destroyed at α ~ Δ , one would expect Δ_S and Δ_B to have similar critical field or close at similar $\mu_0 H$ (or E_Z) because $\Delta_S \approx \Delta_B$ at $\mu_0 H = 0$ T (Fig. 3). When SOC is taken into account, we expect the surface/interface critical field $H_{C,\parallel}^S$ (corresponds to Δ_S) to be even higher, because a stronger SOC is expected at the interface according to Fig. 1B. To estimate the bulk critical field $(H_{C,\parallel}^B)$, we fit the transport data according to Eq. 1 (Fig. 3F, inset), which yields $H_{C,\parallel}^B \sim 8.1 \,\mathrm{T}$ at 300 mK. To estimate $H_{C,\parallel}^S$, we note that it shall be reached shortly after the fill-up of the low-field gap across the transition at $\mu_0 H \sim 3$ T (compared to Fig. 2B). Therefore, we have $H_{C,\parallel}^S < H_{C,\parallel}^B$. Such a stronger depairing on Δ_S cannot be solely explained by $\mu_0 H$, and one needs to consider other depairing mechanisms for the surface/interface.

The stronger depairing of Δ_S shown in Fig. 3E is unusual for a



tor resonators made of ultrathin Au(111)/Nb. (A) ABS energy versus $\mu_0 H$. The energy with uncertainties indicated by the error bar. The peaks shift linearly with $\mu_0 H$ and the straight lines are the linear fit with slopes corresponding to the Landé g-factor g_{eff} bias conductance peak (ZBCP) is formed (Fig. 3B). However, the ZBCP is unstable and g to Fig. 3E. (B) Raman spectroscopy characteristics of the epitaxial trigonal Te tunnel nodes present. The inset shows the crystal structure of trigonal Te and the vibration (5 nm)/Nb (12 nm) layers (Materials and Methods). The inset shows the stack layout sision (S_{21}) measurements signifying the resonance peaks (T=35 mK). (E) Q_i versus $\langle n \rangle$ interfacing Au(111) with the Te barrier. A picture considering $g_{eff} \sim 12$ at Te-Au(111) interface and $g \sim 2$ in bulk Au(111)/Nb is consistent with the combined experimental results in Figs. 2 and 3. Noting that the surface gap closes at $\alpha = \frac{E_Z^2}{\mu_B H_{SO}^8} \sim \Delta_S$ with $E_Z = \frac{1}{2} g_{eff} \mu_B H_{C,\parallel}^S$, we have $H_{C,\parallel}^S \sim \frac{1}{g_{eff}/2} \sqrt{H_P H_{SO}^S}$. Here, H_{SO}^S is H_{SO} at the surface of Au(111) [or at the Te/Au(111) interface], and $H_D = \frac{\Delta_S}{R}$ as defined Fig. 4. ABS demonstrating an enhanced interface Landé g-factor and high Q-factor resonators made of ultrathin Au(111)/Nb. (A) ABS energy versus μ₀H. The energies, or the peak locations of ABS (see also Fig. 3, A and E), are fitted using Gaussians with uncertainties indicated by the error bar. The peaks shift linearly with μ_0H and cross each other at $\mu_0 H \sim \pm 0.5$ T, suggesting that the ABS could be spin polarized. The straight lines are the linear fit with slopes corresponding to the Landé g-factor g_{eff} ~ 12, which is six times larger than $q \sim 2$. At the crossing point ($\mu_0 H \sim \pm 0.5$ T), a zero bias conductance peak (ZBCP) is formed (Fig. 3B). However, the ZBCP is unstable and splits as soon as $\mu_0 H$ increases. The inset shows the low field dl/dV data corresponding to Fig. 3E. (B) Raman spectroscopy characteristics of the epitaxial trigonal Te tunnel barrier. The trigonal Te peaks (A₁, E₁, and E₂) are observed with no other vibration modes present. The inset shows the crystal structure of trigonal Te and the vibration modes. (C) The array of superconductor resonators fabricated using ultrathin Au(111) (5 nm)/Nb (12 nm) layers (Materials and Methods). The inset shows the stack layout of the layers and a zoomed-in image of one resonator. (**D**) Power-dependent transmission (S_{21}) measurements signifying the resonance peaks (T = 35 mK). (**E**) Q_i versus $\langle n \rangle$ for three typical quarter-wave resonators of (C).

To explain $H_{C,\parallel}^S < H_{C,\parallel}^B$, we consider a stronger depairing for Δ_S at the Te/Au(111) interface. Here, we notice that the surface of Au(111) is also the interface between Au(111) and the tunnel barrier Te (Fig. 1C), which can be chiral if it is in the trigonal phase. We rewrite $E_Z = \frac{1}{2} g_{eff} \mu_B H$ with g_{eff} being the effective Landé g-factor, which absorbs all the contributions that enhance the interface E_Z . To find out the relationship $E_Z \sim H$, we focus on the low field regime in Fig. 3E by expanding the field dependence of the in-gap states and replotting it in Fig. 4A (inset). Thanks to the high-quality epitaxial Te barrier with a small Γ (section S2), subtle in-gap states are resolved. These states are expressed as a pair of small dI/dV peaks moving with H in a linear way (Fig. 4A), which suggests that they could be ABS. Moreover, the linear field dependence and the crossing of the peaks (Figs. 3E and 4A) indicate that the states are spin polarized and the change of energy under a magnetic field is $\propto E_Z$. To do a quantitative analysis, we fit the ABS peaks and plot their energy versus H (with error bar) in Fig. 4A. According to $E_Z = \frac{1}{2} g_{eff} \mu_B H$, we have $\Delta E_Z = \frac{1}{2} g_{eff} \mu_B(\Delta H)$. The fitting in Fig. 4A yields $g_{eff} \sim 12$. Such g_{eff} , a sixfold increase compared to $g \sim 2$ in either Au (19) or Nb (20), cannot be explained by any bulk properties of the sample. Because ABS is often an interface effect, the large g_{eff} is likely due to

Au(111) [or at the Te/Au(111) interface], and $H_p = \frac{\Delta_s}{\sqrt{2}\mu_B}$ as defined. According to the thickness dependence in Fig. 1B, $H_{SO}^S > H_P$ is expected at the interface. Therefore, we estimate $H_{C,\parallel}^{S} > \frac{1}{g_{\rm eff}/2} H_{P}$. Taking $H_P \sim 11$ T for $\Delta_S \sim 0.9$ meV ($\Delta_S \approx \Delta_B$), we obtain $H_{C,\parallel}^S > 1.8$ T, consistent with the fast closing of Δ_S as shown in Fig. 3E. The substantially enhanced Landé g-factor, i.e., $g_{eff} \sim 12$, agrees with a spinactive interface, which explains the observed ABS in Figs. 3E and 4A (21, 22). Such an interface is expected to host spin triplet superconductivity (21, 23) and requires a generalized BTK formalism beyond eq. S1 to model (23, 24). The nearly magnetic field-independent dI/dV spectra in Fig. 3D (or after the closing of Δ_S) are very unusual (Fig. 3D), which cannot be simply explained by a superconducting gap following eq. S1 under $\mu_0 H$. In addition, because $H_{C,\parallel}^B \sim 8.1 \text{ T}$ (Fig. 3F), one would expect a substantial gap reduction when $\mu_0 H$ is approaching $H_{C,\parallel}^B$. However, Fig. 3D shows that the gap is nearly unchanged up to $\mu_0 H \sim 8.0$ T and even slightly increased at $\mu_0 H \sim 8.0$ T compared to $\mu_0 H \sim 5.5$ T. Such an unusual superconducting gap (Fig. 3D), robust against $\mu_0 H$, could hint the spin triplet superconductivity.

While we extract g_{eff} using ABS, it is not yet clear why there are spin polarized ABS at $\mu_0 H = 0$ T. In particular, we notice that no magnetic material with a spontaneous magnetization is present. To answer this question, we study the crystal structure of the epitaxially grown Te layer that is used as a tunnel barrier. Using Raman spectroscopy, we observe distinct Raman peaks at $A_1 = 121.15 \text{ cm}^{-1}$, $E_1 = 92.21 \text{ cm}^{-1}$, and $E_2 = 140.64 \text{ cm}^{-1}$ (Fig. 4B), which are characteristic to trigonal Te (25). The vibration modes in correspondence to each of the Raman peaks are illustrated in Fig. 4B (inset). The A₁ mode (the major peak in Fig. 4B) corresponds to the breathing mode of the Te helical chain. We further carry out in situ angledependent reflection high-energy electron diffraction (RHEED) measurements on the Te layer (section S4). The results suggest that the sixfold rotation symmetry of Au(111) facilitates the growth of trigonal Te, which also has sixfold rotation symmetry (Fig. 4B, inset, and section S4). Combining Raman and RHEED results, we conclude that the Te barrier layer, when carefully grown, can be an epitaxial trigonal Te. The helical Te chains in a unit cell (Fig. 4B, inset) may give rise to domains with a distinct chirality. The size of the domain and its crystallinity may depend on the quality of Te and could get enhanced by improving the epitaxial growth. Because the junction has a microscopic area (Materials and Methods), it may help probe a local region of trigonal Te with a distinct chirality on average. Moreover, the ABS is a subtle interface phenomenon; therefore, it may sensitively depend on the interface quality and the chiral domains of Te. Nevertheless, the combination of chiral Te and a superconductor with strong SOC (Fig. 1, B and C) satisfies the needed components for CISS (6–8). Compared to other work where $g \sim 2$ is reported (2, 3), we demonstrate a much larger $g_{eff} \sim 12$, which highlights the spin-active interface and directly points toward CISS. Here, we note that the high-quality interface we created in situ under UHV could be a key factor leading to the substantially enhanced CISS phenomena, whereas in other work, the interface was often created in an ex situ way by the adsorption of organic chiral molecules on the surface of a superconductor (2-5).

To further demonstrate the superconductor heterostructure, Au(111)/Nb has excellent microwave (RF) performance and can potentially be used as a component for superconducting qubits; we fabricate resonators using ultrathin Au(111)/Nb layers (Fig. 4C). We follow the same coplanar waveguide (CPW) design (Materials and Methods) as those used in conventional Nb resonators, which often consisted of Nb layers that are one order of magnitude thicker. We carry out superconducting resonator measurements at 35 mK and find out that Au(111) limits the defect formation, i.e., the formation of uncontrolled Nb oxides, in ultrathin Nb. It has been shown that the native oxides of Nb are the main sources responsible for two-level defects (TLS), i.e., possible trapping sites for quasiparticles, and additional dielectric losses in commonly used transmon qubits, which causes qubit relaxation or decoherence (26, 27). Using resonators fabricated from Au(111)/Nb (Materials and Methods), Fig. 4D shows an example of the sharp microwave resonance peaks observed in transmission near an RF frequency ~5.747 GHz at 35 mK temperature in one of the resonators. The resonance peak

is well-defined with a Lorentzian line shape, which is fit using the established diameter correction method (DCM) (28) to extract internal (Q_i) and external (Q_e) quality factors. An internal quality (Q)-factor $Q_i > 10^6$ is achieved when the averaged microwave photon number $\langle n \rangle$ is large (Fig. 4E). When $\langle n \rangle$ is reduced toward the single-photon limit (Fig. 4E), Q_i decreases to values between 2×10^{5} and 4×10^{5} due to the contribution of saturable TLS to RF power loss (29). We note that the narrow conductor/gap dimensions in our CPW resonator design will result in lower Q_i values than designs with larger dimensions, which dilute the participation of surfaces and interfaces (Materials and Methods). The Q_i values observed near and below single-photon powers in these chips are comparable to values obtained in conventional resonators with one order of magnitude thicker Nb films (100 nm) based on a similar CPW design on sapphire (section S6 and fig. S7). This suggests that these high-quality Au(111)/Nb structures perform well even for these ultrathin (12 nm) Nb layers and are suited for use in superconducting qubits such as transmons. In addition, the high Q_i values observed suggest that Au(111) limits the defects in Nb, thereby resulting minimal in-gap states.

DISCUSSION

In conclusion, we have demonstrated an enhanced Zeeman field at the Te(trigonal)/Au(111) interface giving rise to $g_{e\!f\!f}^S\sim 12.$ Such an enhanced interface Zeeman field closes the surface superconducting gap of Au(111) while maintaining the bulk superconductivity, thereby providing an alternative route to creating a unique surface/interface superconductor. One may exploit such locally enhanced Zeeman field to construct a nanostructured topological superconductor (TSC) by patterning, for example, nanowires of trigonal Te over Au(111) (10, 11). The Te layer may, at the same time, serve as a high-quality tunnel barrier, making it advantageous in fabricating multi-terminal planar tunneling devices involving TSC (30, 31). An epitaxially grown Te layer in its trigonal form on Au(111)/Nb could also be useful for superconducting spintronics. In addition, we have demonstrated a substantially enlarged Δ_S (Fig. 3), with a several-fold increase compared to the prior report (13), achieving $\Delta_S \approx \Delta_B$ in 5-nm Au(111) grown on Nb. Theory simulations have shown that a larger surface superconducting gap may result in a larger topological gap giving rise to a robust TSC (10, 12). Moreover, $\Delta_S \approx \Delta_B$ ensures that the whole Au(111) layer is fully gapped, which limits microwave loss due to quasiparticle excitations across the gap, as well as reducing TLS defects that lead to dielectric losses. These are essential for applying Au(111)/Nb in microwave resonators and superconducting qubits.

MATERIALS AND METHODS

The Au(111)/Nb bilayers are grown using molecular bean epitaxy. The Nb layer thickness can be controlled down to a few nanometers and the Au(111) layer thickness down to a few angstroms. Following the growth, Au(111)/Nb samples are routinely taken out of the UHV chamber for transport and tunneling measurements in an Oxford 3He Heliox cryostat. The point contact spectroscopy is carried out using a normal metal (gold) wire touching the sample surface forming a junction with a controlled tunnel barrier layer (Te or Se) added. The point contact wire is made in a way to allow four-terminal differential conductance (dI/dV) measurement through the junction (Fig. 1C, inset). The junction usually has an area of

~20 µm in diameter. dI/dV measurement is performed at a temperature of ~300 mK with a modulation voltage $\leq k_BT$.

The Au(111)/Nb CPW resonators are fabricated following a standard design consisting of eight inductively coupled quarter-wave resonators in a "hanger" configuration with resonances falling between 4 and 8 GHz using standard photolithography steps and Ar ion milling. The CPW design chosen has conductor/gap dimensions of 6 μm/3 μm. These narrow dimensions are chosen to increase the participation of the surfaces and interfaces, thus making the loss measurement more sensitive to their contribution (32). After resonator fabrication, the chip was installed in a Au-plated Cu sample package using Al wire bonds. RF characterization of frequency multiplexed CPW resonators was performed in a dilution refrigerator having a base temperature of 35 mK. Each chip having dimensions 7.5 mm × 7.5 mm contains eight frequency-multiplexed quarterwave hanger resonators with a central feedline. Power-dependent transmission (S_{21}) measurements were performed at base temperature spanning powers corresponding to ~10⁶ to ~0.1 photon occupation in the resonator. Each resonator is measured using a vector network analyzer, and the Lorentzian spectra are fit using the established DCM to extract internal and coupling quality factors (Q_i and Q_{ρ}) as a function of photon number (28). The signal and amplifier chain used is similar to that outlined previously (32) with amplifiers installed at 4 K and at room temperature. A Josephson parametric amplifier installed at the mixing chamber (35 mK) was used for all low-power measurements (below ~10³ photon occupation).

For sample structure characterizations, ex situ x-ray—based analyses are performed using a Rigaku GIXRD system. In situ RHEED is carried out using a 7.5-mW electron beam. Ex situ Raman spectroscopy is carried out using a Horiba LabRam system, in which a 532-nm unpolarized excitation laser with a 100- μ m spot size was used to scan the films.

Supplementary Materials

This PDF file includes: Sections S1 to S6 Figs. S1 to S7

Table S1 References

REFERENCES AND NOTES

- R. Nakajima, D. Hirobe, G. Kawaguchi, Y. Nabei, T. Sato, T. Narushima, H. Okamoto, H. M. Yamamoto, Giant spin polarization and a pair of antiparallel spins in a chiral superconductor. *Nature* 613, 479–484 (2023).
- H. Alpern, K. Yavilberg, T. Dvir, N. Sukenik, M. Klang, S. Yochelis, H. Cohen, E. Grosfeld, H. Steinberg, Y. Paltiel, O. Millo, Magnetic-related states and order parameter induced in a conventional superconductor by nonmagnetic chiral molecules. *Nano Lett.* 19, 5167–5175 (2019).
- T. Shapira, H. Alpern, S. Yochelis, T. K. Lee, C. C. Kaun, Y. Paltiel, G. Koren, O. Millo, Unconventional order parameter induced by helical chiral molecules adsorbed on a metal proximity coupled to a superconductor. *Phys. Rev. B* 98, 214513 (2018).
- H. Alpern, M. Amundsen, R. Hartmann, N. Sukenik, A. Spuri, S. Yochelis, T. Prokscha, V. Gutkin, Y. Anahory, E. Scheer, J. Linder, Z. Salman, O. Millo, Y. Paltiel, A. Di Bernardo, Unconventional Meissner screening induced by chiral molecules in a conventional superconductor. *Phys. Rev. Mater.* 5, 114801 (2021).
- Z. Wan, G. Qiu, H. Ren, Q. Qian, D. Xu, J. Zhou, J. Zhou, B. Zhou, L. Wang, Y. Huang, K. L. Wang, X. Duan, Signatures of chiral superconductivity in chiral molecule intercalated tantalum disulfide. arXiv:2302.05078 [cond-mat.supr-con] (2023).
- Y. Adhikari, T. Liu, H. Wang, Z. Hua, H. Liu, E. Lochner, P. Schlottmann, B. Yan, J. Zhao, P. Xiong, Interplay of structural chirality, electron spin and topological orbital in chiral molecular spin valves. *Nat. Commun.* 14, 5163 (2023).
- Y. Liu, J. Xiao, J. Koo, B. Yan, Chirality-driven topological electronic structure of DNA-like materials. Nat. Mater. 20, 638–644 (2021).

- Q. Yang, Y. Li, C. Felser, B. Yan, Chirality induced spin selectivity in chiral crystals. arXiv:2312.04366v2 [cond-mat.mes-hall] (2024).
- M. Amundsen, J. Linder, J. W. A. Robinson, I. Žutić, N. Banerjee, Colloquium: Spin-orbit effects in superconducting hybrid structures. *Rev. Mod. Phys.* 96, 021003 (2024).
- Y.-M. Xie, K. T. Law, P. A. Lee, Topological superconductivity in EuS/Au/superconductor heterostructures. *Phys. Rev. Res.* 3, 043086 (2021).
- M. Papaj, L. Fu, Creating Majorana modes from segmented Fermi surface. Nat. Commun. 12, 577 (2021).
- S. Manna, P. Wei, Y. Xie, K. T. Law, P. A. Lee, J. S. Moodera, Signature of a pair of Majorana zero modes in superconducting gold surface states. *Proc. Natl. Acad. Sci. U.S.A.* 117, 8775–8782 (2020).
- P. Wei, S. Manna, M. Eich, P. Lee, J. Moodera, Superconductivity in the surface state of noble metal gold and its Fermi level tuning by EuS dielectric. *Phys. Rev. Lett.* 122, 247002 (2019).
- P. Wei, F. Katmis, C. Z. Chang, J. S. Moodera, Induced superconductivity and engineered josephson tunneling devices in epitaxial (111)-oriented gold/vanadium heterostructures. *Nano Lett.* 16, 2714–2719 (2016).
- 15. M. Tinkham, Introduction to Superconductivity: Second Edition (Dover Publications, 2004).
- N. R. Werthamer, E. Helfand, P. C. Hohenberg, Temperature and purity dependence of the superconducting critical field, H_{c2}. III. Electron spin and spin-orbit effects. *Phys. Rev.* 147, 295–302 (1966).
- M. Hirayama, R. Okugawa, S. Ishibashi, S. Murakami, T. Miyake, Weyl node and spin texture in trigonal tellurium and selenium. *Phys. Rev. Lett.* 114, 206401 (2015).
- A. C. Potter, P. A. Lee, Topological superconductivity and Majorana fermions in metallic surface states. Phys. Rev. B 85, 094516 (2012).
- V. I. Smelyansky, M. J. G. Lee, J. M. Perz, Relativistic calculation of conduction-electron q-factors in noble metals. J. Phys. Condens. Matter 5, 6061 (1993).
- D. C. Vier, S. Schultz, Observation of conduction electron spin resonance in both the normal and superconducting states of niobium. *Phys. Lett. A* 98, 283–286 (1983).
- I. Žutić, S. Das Sarma, Spin-polarized transport and Andreev reflection in semiconductor/ superconductor hybrid structures. *Phys. Rev. B* 60, R16322–R16325 (1999).
- D. Beckmann, F. Hübler, M. J. Wolf, H. Löhneysen, Andreev bound states at spin-active interfaces. *Philos. Trans. A Math Phys. Eng. Scio.* 376, 20150002 (2018).
- T. Vezin, C. Shen, J. E. Han, I. Žutić, Enhanced spin-triplet pairing in magnetic junctions with s-wave superconductors. *Phys. Rev. B* 101, 014515 (2020).
- R. Cai, Y. Yao, P. Lv, Y. Ma, W. Xing, B. Li, Y. Ji, H. Zhou, C. Shen, S. Jia, X. C. Xie, I. Žutić, Q. F. Sun, W. Han, Evidence for anisotropic spin-triplet Andreev reflection at the 2D van der Waals ferromagnet/superconductor interface. *Nat. Commun.* 12, 6725 (2021).
- Y. Wang, G. Qiu, R. Wang, S. Huang, Q. Wang, Y. Liu, Y. du, W. A. Goddard III, M. J. Kim, X. Xu, P. D. Ye, W. Wu, Field-effect transistors made from solution-grown two-dimensional tellurene. *Nat. Electron* 1, 228–236 (2018).
- S. E. de Graaf, L. Faoro, L. B. Ioffe, S. Mahashabde, J. J. Burnett, T. Lindström, S. E. Kubatkin, A. V. Danilov, A. Y. Tzalenchuk, Two-level systems in superconducting quantum devices due to trapped quasiparticles. Sci. Adv. 6, eabc5055 (2020).
- A. P. M. Place, L. V. H. Rodgers, P. Mundada, B. M. Smitham, M. Fitzpatrick, Z. Leng, A. Premkumar, J. Bryon, A. Vrajitoarea, S. Sussman, G. Cheng, T. Madhavan, H. K. Babla, X. H. Le, Y. Gang, B. Jäck, A. Gyenis, N. Yao, R. J. Cava, N. P. de Leon, A. A. Houck, New material platform for superconducting transmon qubits with coherence times exceeding 0.3 milliseconds. *Nat. Commun.* 12, 1779 (2021).
- M. S. Khalil, M. J. A. Stoutimore, F. C. Wellstood, K. D. Osborn, An analysis method for asymmetric resonator transmission applied to superconducting devices. J. Appl. Phys. 111, 054510 (2012).
- J. M. Martinis, K. B. Cooper, R. McDermott, M. Steffen, M. Ansmann, K. D. Osborn, K. Cicak, S. Oh, D. P. Pappas, R. W. Simmonds, C. C. Yu, Decoherence in Josephson qubits from dielectric loss. *Phys. Rev. Lett.* 95, 210503 (2005).
- J. S. Moodera, P. A. Lee, P. Wei, S. Manna, Majorana pair based qubits for fault tolerant quantum computing architecture using superconducting gold surface states. U.S. Patent US20200356887A1 (2020).
- S. Vijay, L. Fu, Teleportation-based quantum information processing with Majorana zero modes. Phys. Rev. B 94, 235446 (2016).
- C. R. H. McRae, H. Wang, J. Gao, M. R. Vissers, T. Brecht, A. Dunsworth, D. P. Pappas, J. Mutus, Materials loss measurements using superconducting microwave resonators. *Rev. Sci. Instrum.* 91, 091101 (2020).
- J. E. Mahan, K. M. Geib, G. Y. Robinson, R. G. Long, A review of the geometrical fundamentals of reflection high-energy electron diffraction with application to silicon surfaces. J. Vac. Sci. Technol. A 8, 3692–3700 (1990).
- 34. J. Daillant, A. Gibaud, X-ray and Neutron Reflectivity: Principles and Applications, vol. 770 of Lecture Notes in Physics (Springer, 2009).
- G. E. Blonder, M. Tinkham, T. M. Klapwijk, Transition from metallic to tunneling regimes in superconducting microconstrictions: Excess current, charge imbalance, and supercurrent conversion. *Phys. Rev. B* 25, 4515–4532 (1982).

SCIENCE ADVANCES | RESEARCH ARTICLE

 R. C. Dynes, V. Narayanamurti, J. P. Garno, Direct measurement of quasiparticle-lifetime broadening in a strong-coupled superconductor. *Phys. Rev. Lett.* 41, 1509–1512 (1978).

Acknowledgments: We thank J. Shi for the support on 3He millikelvin temperature measurements. We thank C. R. McRae for the discussions on superconductor resonators. Funding: C.C., J.T., E.-D.C., D.M., V.S., and P.W. would like to acknowledge the support from NSF CAREER DMR2046648. P.A.L., J.S.M., and P.W. would like to acknowledge the support from NSF Convergence Accelerator Track-C ITE-2040620. J.S.M. and P.W. would like to acknowledge the Lincoln Lab Line fund. Y.H. and J.S.M. would like to acknowledge National Science Foundation NSF-DMR 1700137 and 2218550, Office of Naval Research N00014-20-1-2306, Army Research Office W911NF-20-2-0061 and DURIP W911NF-20-1-0074, and the Center of Integrated Quantum Materials NSF-DMR 1231319. P.A.L. would like to acknowledge the support by DOE office of Basic Sciences grant no. DE-FG0203ER46076. Author contributions: C.C., J.T., and V.S. synthesized the bilayer thin films. C.C. and J.T. carried out tunneling and transport measurements. K.S. performed GIXRD measurements and data analysis. D.M. and V.S.

fabricated the resonator devices. A.M. and R.S. performed microwave absorption measurements. E.-D.C. performed Raman measurements and analysis. P.W. oversaw the project and designed the research with the discussions from J.A., P.A.L., and J.S.M. All authors contributed to writing the manuscript. **Competing interests**: P.W. is the inventor on a provisional patent filed by the University of California, Riverside (serial no. 63/646657). J.A. is an employee of Quantum Circuits Inc. in New Haven, CT. All other authors declare that they have no competing interests. **Data and materials availability:** All data needed to evaluate the conclusions in the paper are present in the paper and/or the Supplementary Materials. The data will be publicly accessed on Dryad under the link: https://doi.org/10.5061/dryad.4xgxd25jf.

Submitted 4 February 2024 Accepted 19 July 2024 Published 23 August 2024 10.1126/sciadv.ado4875